RESEARCH ARTICLE | FEBRUARY 09 2026

A new framework for confined high-speed gas–liquid microfluidics: Developing region effect on instability

Zihao Meng ; Carlos Hidrovo

Physics of Fluids 38, 022006 (2026)
https://doi.org/10.1063/5.0304622

Physics of Fluids ARTICLE pubs.aip.org/aip/pof

A new framework for confined high-speed gas–liquid microfluidics: Developing region effect on instability

Cite as: Phys. Fluids **38**, 022006 (2026); doi: 10.1063/5.0304622
Submitted: 30 September 2025 · Accepted: 21 January 2026 ·
Published Online: 9 February 2026

View Online Export Citation CrossMark

Zihao Meng[a] and Carlos Hidrovo

AFFILIATIONS

Mechanical and Industrial Engineering Department, Northeastern University, Boston, Massachusetts 02115, USA

[a]Author to whom correspondence should be addressed: meng.zih@northeastern.edu

ABSTRACT

Predicting droplet generation dynamics in confined coaxial jets in droplet microfluidics can be challenging, especially for gas–liquid systems. This is particularly true when trying to assess the droplet size and generation rate based on perturbation and instrument parameter analysis. Extensive measurements of jet radii across a wide range of flow conditions suggest that the commonly held assumption that the jet is fully developed over most of its length and at droplet breakup might not be accurate for gas–liquid systems. In contrast, the entrance or developing region appears to have a substantial influence on the instability of these systems, and jet breakup frequently occurs before the jet radius reaches its fully developed value. A scaling analysis was employed to examine the developing region of confined coaxial jets. The results revealed that the length of the developing region is primarily determined by the difference between the Capillary numbers of the inner and outer flows, with a larger difference leading to a shorter distance required for the jet to converge toward its fully developed radius. The scaling results further indicate that the developing region can be divided into an inertia-controlled region near the inlet and a viscosity-controlled region downstream, referred to as region II, which occupies the major portion of the developing region. Based on the scaling results, a pseudo-fully developed assumption was introduced for region II, and a dispersion relation specifically for the developing region was proposed. The unknown coefficients arising from the scaling formulation were determined using experimentally measured regime boundaries, allowing the dispersion relation to consistently account for variations in channel geometry. Compared to existing dispersion relations derived under fully developed assumptions, this improved approach significantly enhances the accuracy of predicting jet breakup frequencies, as validated by experimental measurements.

I. INTRODUCTION

Droplet microfluidics is a lab-on-a-chip technology that enables the high-throughput generation of micro- to nanoscale droplets through flow manipulation in microchannels.[1] Due to advantages, such as high droplet uniformity,[2] high surface-to-volume ratio,[3] and low production cost,[4] this technology has been widely applied in drug delivery,[5,6] high-throughput drug and cell screening,[7,8] parallel cell reactors,[9,10] as well as biochemical indicator sensing.[11]

The essence of droplet microfluidics is the use of an auxiliary continuous-phase fluid to disperse a target fluid (the dispersed phase) into droplets within microchannels.[12] One common approach is to form a coaxial co-flow configuration, where the dispersed phase occupies the central axis (inner flow), and the continuous phase occupies the region from the dispersed-phase interface to the microchannel wall (outer flow). For simplicity of notation, the inner flow is designated by subscript 1, while the outer flow is designated by subscript 2.

The breakup of a continuous jet into dispersed droplets, liquid films, or sprays under the influence of surface tension is a phenomenon widely observed in scientific research and in everyday life, and its underlying mechanism has long been studied. Plateau[13] was the first to observe and describe this behavior, which was later explained by Rayleigh[14] on the basis of the principle of minimizing surface energy. In 1990, Huerre[15] introduced instability theory into this domain, providing not only a dynamic perspective to reinterpret the phenomenon in terms of perturbation growth but also offering precise mathematical and physical interpretations of flow regimes, such as Dripping (Absolutely Unstable) and Jetting (Convectively Unstable). Building on this foundational work, Guillot,[16,17] Herrada,[18] and others[19–22] derived dispersion relations for confined coaxial jets that have since played a critical role in predicting key characteristics in droplet microfluidics, including throughput,[23,24] droplet size,[25] and polydispersity.[26]

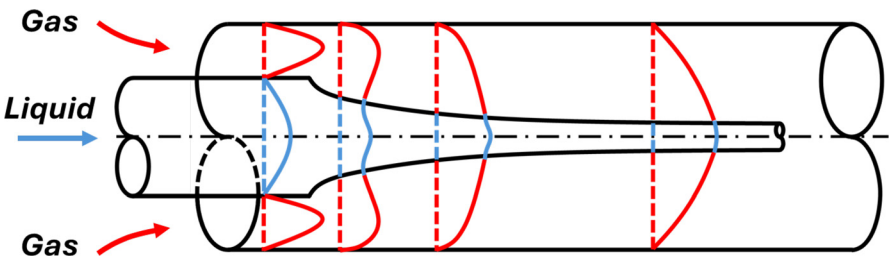

FIG. 1. Sketch of the interface evolution and velocity distribution development in a confined coaxial jet system.

The success of these theoretical studies has led to significant advancements and extensive exploration of droplet microfluidics over the past decade.[27] However, these efforts have primarily focused on liquid–liquid systems, with high-viscosity liquids (typically oils)[28,29] as the continuous phase. Droplet formation in these systems is primarily driven by viscous forces, allowing stable production of highly uniform droplets, though generally limited to generation rates below 10 kHz.[30] Recently, a newer alternative has been proposed that utilizes gas as the continuous phase, where high-speed gas flow through microchannels achieves droplet formation via mechanisms distinctly different from liquid–liquid systems.[11,26,31,32] Due to their high-speed nature, these systems can achieve significantly higher throughput in the range of 10 kHz–1 MHz[33] and produce smaller droplets (sub-micron level),[26,34,35] albeit typically at the expense of reduced droplet uniformity.[26,34] While liquid breakup can indeed be induced by high-speed coaxial airflow in open-air configurations,[36,37] such approaches and confined microchannel-based methods address fundamentally different application scenarios. Open-air atomization is well suited for spray generation and aerosolization, but it typically involves strong three-dimensional (3D) instabilities, limited control over breakup location, and significant sensitivity to environmental conditions. In contrast, confined gas–liquid microchannels provide a closed and geometrically controlled environment that enables straightforward integration with microfluidic platforms. This confinement is particularly advantageous for applications requiring on-chip integration, precise control of droplet generation, and high reproducibility. In addition, closed microchannel systems reduce the release of specialized or hazardous gases into the environment, which is critical for applications involving reactive or trace gases. Such configurations are also employed in gas-borne particle detection and analysis,[11] where confinement prevents cross-contamination between the sample gas and ambient air. For these reasons, the present study focuses on confined gas–liquid microflows, where the role of the developing region can be systematically investigated within a controlled and application-relevant framework.

However, significant discrepancies in frequency prediction arise when the existing dispersion relations are applied to gas–liquid systems, especially under high gas flow rates.

It is evident that, for any given combination of flow rates within a defined channel dimension, the flow will eventually reach a fully developed state at a sufficiently large distance downstream, as illustrated in Fig. 1, assuming no external disturbances. Observing the cylindrical interface between the two fluids, the so-called developing region becomes apparent, defined as the region where the radius of this interface transitions from its initial condition to a fully developed state. This study reveals that the developing region can be subdivided into two distinct zones: an inertia-dominated region, characterized by rapid changes in radius, and a viscosity-dominated region, where changes in radius occur more gradually. Because of the typically lower viscosity of gases compared to liquids, the length of the developing region (LDR) in gas–liquid systems significantly exceeds that of liquid–liquid systems. Consequently, the widely accepted assumption in liquid–liquid systems—that jet breakup occurs within the fully developed region—no longer holds true in gas–liquid systems, as illustrated in Fig. 2.

Our experiments carried out in seven different channel geometries consistently confirmed this finding. This finding also implies that existing dispersion relations are fundamentally inadequate to provide the mathematical foundation needed for further advances in gas–liquid microfluidic systems. It is, therefore, essential to develop new theoretical models and dispersion relations that specifically account for the developing region of confined coaxial jets.

The definitions of symbols and parameters used throughout this paper are summarized in the nomenclature.

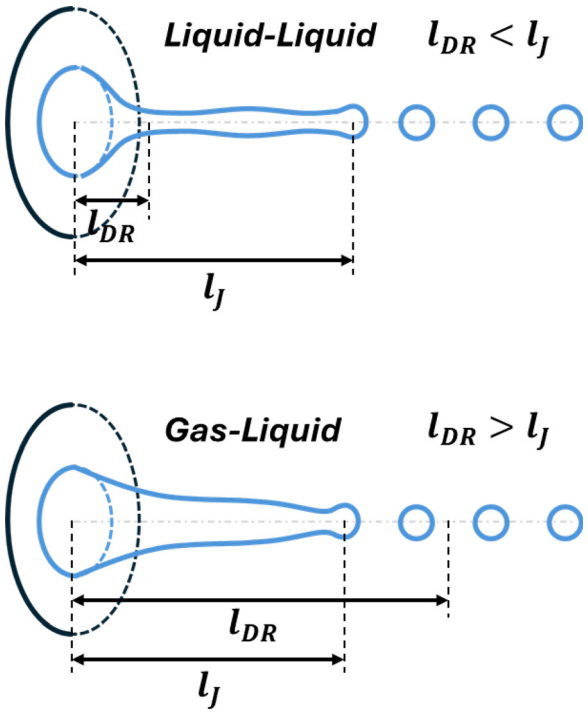

FIG. 2. Comparison of the developing region lengths and jet breakup positions in different confined coaxial jet systems (l_{DR} vs l_J): in liquid–liquid systems, the jet radius rapidly converges to the fully developed state, and breakup occurs within the fully developed region; in gas–liquid systems; the convergence of jet radius is slower, and breakup occurs upstream of the fully developed region.

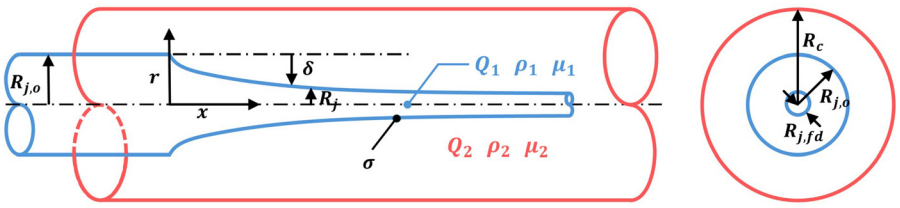

FIG. 3. Sketch of a confined coaxial jet system in cylindrical coordinates, illustrating the inner flow (1), outer flow (2), cylindrical channel dimensions, and relevant flow/physical parameters.

II. THEORETICAL MODELING

A. Modeling of developing region

As shown in Fig. 3, the inner and outer phases of a confined coaxial jet meet at the inlet ($x = 0$) and gradually evolve downstream toward a fully developed state. The most prominent indicator of this transition is the variation in the radius of the cylindrical interface formed between the two phases along the flow direction, referred to in this study as the "jet radius." As the jet extends downstream, this radius progressively approaches a stable value, marking the onset of fully developed flow.

If the intermediate developing region is conceptually isolated, one can solve separately for the flow fields at the inlet and fully developed states. At the inlet, the flow takes the form of Poiseuille flow in a circular and an annular tube, respectively. At the other end, one obtains the velocity profile shown on the far downstream of Fig. 1 and the corresponding analytical expression, Eq. (1), which shows that the fully developed jet radius can be expressed solely as a function of the flow rates Q_1, Q_2, and the outer channel radius, independent of both the pressure drop and the inlet radius of the inner flow. In other words, it is possible to maintain constant flow rates while modifying the liquid inlet radii, thereby producing completely different jet developing behaviors.

$$\frac{R_{j,fd}}{R_c} = \left(\frac{Q_1}{Q_2} + 1 - \sqrt{\frac{\mu_2 Q_1}{\mu_1 Q_2} + 1}\right)^{1/2} \left(-\frac{\mu_2}{\mu_1} + \frac{Q_1}{Q_2} + 2\right)^{-1/2}. \quad (1)$$

From another perspective, close observation of the fully developed velocity profile reveals that at the interface, the inner flow experiences a viscous force directed opposite to the mean flow direction, while the outer flow surface is dragged forward. Although this may seem counterintuitive, it becomes clear when considering that the pressure drop must be identical in both phases in the fully developed region (since the Laplace pressure is constant across the fixed radius interface). If the inner flow is dragged forward at the interface, the inner pressure drop would become negative, contradicting this balance.

Therefore, it can be inferred that when the inlet flow differs significantly from the fully developed flow, such as in gas–liquid systems where the outer flow velocity greatly exceeds the inner flow velocity, intense flow adjustment must occur in the developing region. There is no physical basis to assume that this adjustment is trivial. In fact, it is reasonable to assume that this region may extend far downstream, especially in the case of gas–liquid systems. This assumption is further confirmed by our experimental results. As shown in Fig. 4, seven datasets from different microchannel geometries reveal that the measured jet diameters far exceed the fully developed theoretical radius, indicating that all jets remain within the developing region.

Compared with the detailed velocity profile, the primary concern lies in the variation of the radius and length of the developing region. To address this, a concise and efficient scaling analysis is adopted. Starting from the Navier–Stokes equations, all variables in the equations are first replaced by the following characteristic scales: x-velocity: $v_x \to u$; r-velocity: $u_r \to v$; spatial parameters: $x \to x$ and $r \to \delta$; pressure: $P \to \rho u^2$. After substitution into the continuity equation, the first scaling relation can be obtained as follows:

$$v_n \sim u_n \frac{\delta}{x}. \quad (2)$$

By substituting Eq. (2) into the equations of x-momentum and r-momentum, respectively, and assuming $\delta \sim x$, corresponding to the region adjacent to the inlet, the simplified expressions for the pressure gradient can be obtained in the inner and outer flows as follows:

$$\frac{\partial P_n}{\partial r} \sim \rho_n u_n^2 \frac{\delta}{x^2} + \frac{\mu_n u_n}{\delta x}, \quad (3)$$

$$\frac{\partial P_n}{\partial x} \sim \frac{\rho_n u_n^2}{x} + \frac{\mu_n u_n}{x^2} + \frac{\mu_n u_n}{\delta^2}. \quad (4)$$

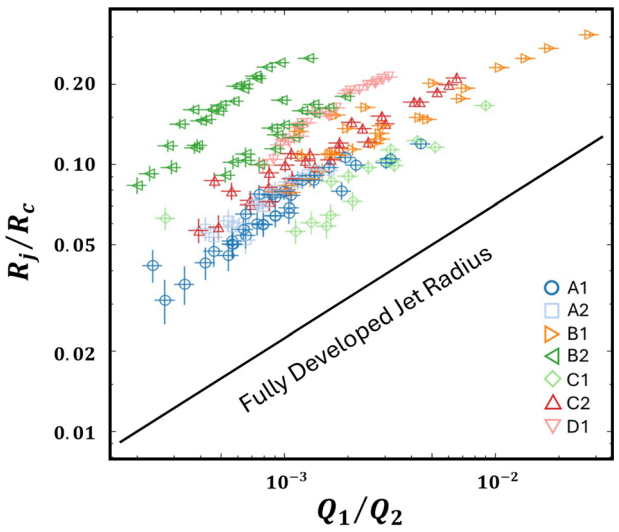

FIG. 4. Log–log plot of normalized jet radius vs inner-to-outer flow rate ratio. Each set of scatter point represents a measurement from one of seven different microfluidic chip designs, with detailed channel geometries provided in Table I in Appendix A. The black solid line indicates the theoretical jet radius in the fully developed state. All measured jet radii exceed this theoretical value. Considering that all jets observed in these experiments are contracting jets, it can be inferred that jet breakup occurs within the developing region.

For high-speed gas–liquid systems, where $Re_x \gg 1$, the expressions can be further simplified as

$$\frac{\partial P_n}{\partial x} \sim \frac{\partial P_n}{\partial r} \sim \rho_n u_n^2 \frac{\delta}{x^2}. \tag{5}$$

Then, by invoking the Laplace pressure, the relationship between the inner and outer pressures is established as follows:

$$P_{1,s} - P_{2,s} \sim \frac{\sigma}{\delta}, \tag{6}$$

$$\frac{dP_{1,s}}{dx} - \frac{dP_{2,s}}{dx} \sim \frac{\sigma}{x\delta}. \tag{7}$$

By substituting the pressure scales Eq. (5) into Eq. (7), we obtain the relationship between δ and x, where both δ and x are normalized as $\tilde{\delta} = \frac{\delta}{R_{j,o}}$ and $\tilde{x} = \frac{x}{R_{j,o}}$,

$$\tilde{\delta} \sim (\Delta We^{-1} \cdot \tilde{x})^{1/2}. \tag{8}$$

It can be seen that in this region ($\delta \sim x$), δ is mainly governed by the difference in the Weber number (ΔWe), where $We = \frac{\rho u^2 R_{j,o}}{\sigma}$ and $\Delta We = We_1 - We_2$.

Similarly, by applying condition $x \gg \delta$ to the momentum equations, we can analyze the flow further downstream. In this region, the flow is approximately one-dimensional, leading to a more gradual variation in jet radius and pressure that changes only along the x-direction. The pressure term obtained from scaling analysis under this condition can be expressed as

$$\frac{dP_n}{dx} \sim \frac{\mu_n u_n}{\delta^2}. \tag{9}$$

Since the variation of R_j along the x direction is gradual, the dominant contribution to the Laplace pressure arises from the curvature of the cylindrical surface. Therefore, Eqs. (6) and (7) are modified as follows:

$$P_1 - P_2 \sim \frac{\sigma}{R_j}, \tag{10}$$

$$\frac{dP_2}{dx} - \frac{dP_1}{dx} \sim \frac{\sigma \frac{dR_j}{dx}}{R_j^2} \sim \frac{\delta\sigma}{xR_{j,o}^2}. \tag{11}$$

In contrast to Eq. (8), the radius variation in this region is primarily governed by the difference in the Capillary number (ΔCa), as shown in the following equation, where $Ca = \frac{\mu u}{\sigma}$ and $\Delta Ca = Ca_1 - Ca_2$

$$\tilde{\delta} \sim (\Delta Ca \cdot \tilde{x})^{1/3}. \tag{12}$$

The scaling results indicate that the evolution of the jet radius transitions from a Weber number dominated region to a Capillary number dominated region, depending on the downstream position of the jet. This transition suggests an evolution of the dominant physical mechanism in the flow development process, from inertia-dominated to viscosity-dominated, as shown in Fig. 5. To further examine flow characteristics within the developing region and to validate the scaling results, CFD simulations were conducted using COMSOL. Water and air were simulated in a microchannel with realistic dimensions. By adjusting the flow parameters and surface tension, convective instabilities in the numerical framework were suppressed, enabling the computation of jets that remained unbroken and free from significant disturbances over a sufficiently long downstream distance.

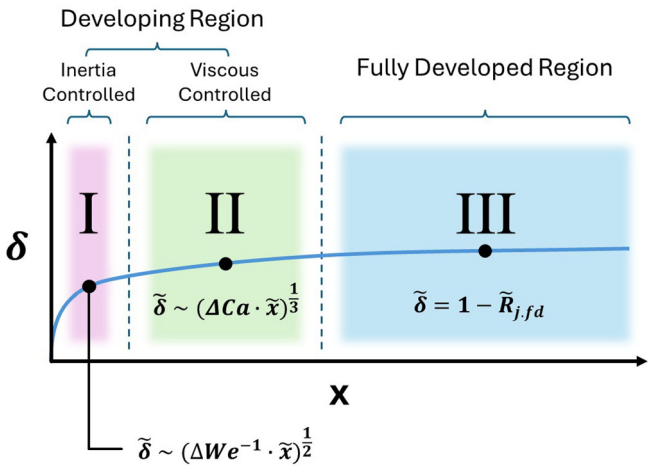

FIG. 5. Schematic illustration of the jet development process proposed in this study. The confined gas–liquid jet evolves through three distinct regions, denoted as region I, region II, and region III. The regions are distinguished based on the evolution of the jet radius along the flow direction, represented by the change of radius δ on the vertical axis. Key characteristics associated with each region are indicated in the schematic.

Analysis of the velocity distribution, pressure drop, and phase interface position and its slope indicates that the COMSOL computations support the hypothesis of an extended developing region in gas–liquid microfluidic jets. The results also corroborate the inertia-viscosity transition inferred from the scaling analysis. Figure 6 presents the COMSOL results, with the velocity profiles and pressure drop shown on the left and the phase interface position together with its slope shown on the right. When the velocity distribution and pressure drop are examined together, strong variations are observed over a short region immediately downstream of the inlet where the inner and outer phases first meet. In this region, the outer flow, which carries higher inertia, experiences a rapid pressure decrease accompanied by a sharp contraction of the jet radius. Momentum is rapidly transferred from the outer flow to the inner flow across the interface to speed up the inner flow. The pressure of the inner flow increases briefly and then begins to decrease, indicating a weakening of momentum transfer.

Downstream of this region, both the velocity profiles and the jet radius transition from rapid variation toward a more stable configuration, indicating the onset of a different developing region. This extended region provides direct numerical support for the pseudo fully developed assumption that is very important and will be adopted in the dispersion analysis later, in the sense that the velocity profile is fully developed like, while the jet radius and pressure gradients continue to relax slowly toward their fully developed values. The persistence of this developing behavior is evidenced by the mismatch between the pressure drops of the inner and outer flows and by the continued variation in the slope of the phase boundary. Within this region, the flow undergoes a transition from inertia controlled to viscosity controlled behavior, consistent with the scaling analysis. As a result, the jet radius

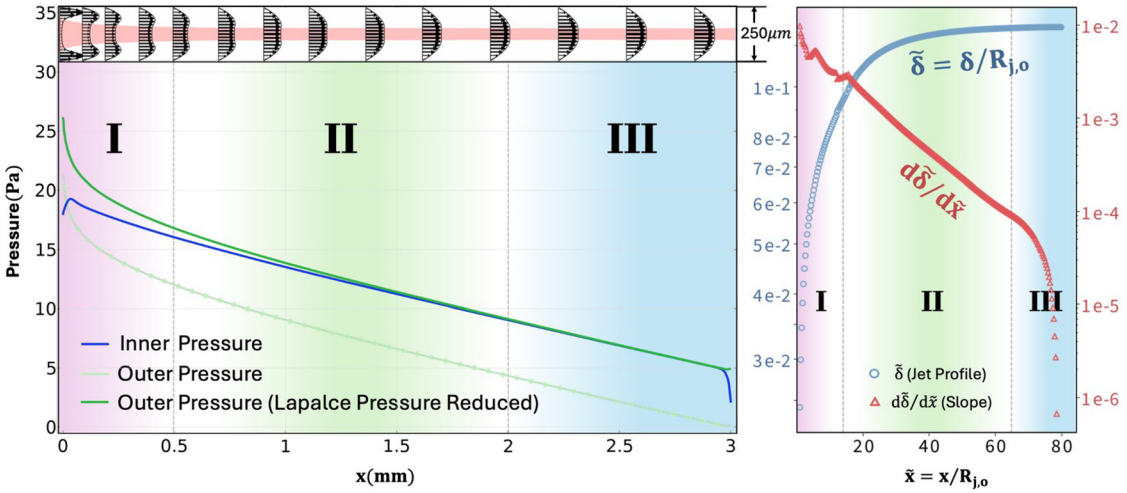

FIG. 6. COMSOL simulation results of a confined gas–liquid jet. The left panel shows the jet interface position in the channel and the streamwise pressure variation of the inner and outer phases. The right panel shows the logarithmic nondimensional change of jet radius $\tilde{\delta}$ and the logarithmic variation of its streamwise slope.

adjusts gradually, and the pressure gradients converge slowly, with fully developed state reached at a downstream distance of approximately sixty times the initial jet radius.

Based on the analysis and validation above, the developing behavior of the confined gas–liquid coaxial jet is divided into three regions, referred to as region I, region II, and region III, as shown in Figs. 5 and 6. Region III corresponds to the fully developed region, while regions I and II together define the developing region. Region I, the inertia-controlled region, is characterized by its small size but drastic variation in jet radius. The evolution of the radius is described by Eq. (8). Region II, the viscosity-controlled region, is described by Eq. (12). In region II, the velocity profile stays a "fully developed-like" profile, and the jet radius changes more gradually, transitioning from near-developed to fully developed values. Unlike region I, region II can extend over a much longer distance and, thus, constitutes the major portion of the developing region.

Based on the underlying assumptions, the scaling in region I arises from the rapid variation of the jet radius, which introduces a strong transverse curvature of the jet interface and the associated Laplace pressure. The scaling represented by Eq. (8) gradually loses validity as the flow develops downstream. By constraining the jet radius variation δ to remain of the same order as the streamwise distance x, the characteristic length scale of region I can be obtained, leading to the estimate of LDR_I given in Eq. (13). Similarly, by setting $\tilde{\delta}$ to $O(\tilde{\delta}_{fd})$ in Eq. (12), corresponding to the convergence toward the fully developed radius, the characteristic length scale of regions I and II combined can be estimated, as shown in Eq. (14),

$$LDR_I \sim \frac{R_{j,o}}{\Delta We}, \tag{13}$$

$$LDR_{I+II} \sim \frac{R_{j,o}}{\Delta Ca} \cdot O(\tilde{\delta}_{fd})^3. \tag{14}$$

It should be noted that Eqs. (13) and (14) are not exact expressions, but they provide an estimate of the LDRs based on scaling considerations. That is, when the Ca values of the inner and outer flows are very close, the distance required for the jet radius to converge becomes significantly longer. This is one of the key differences between gas–liquid and liquid–liquid systems. By putting in the actual numbers measured in the experiments, LDR_I is calculated to range from 6 to 280 μm with an average of 26 μm. For LDR_{I+II}, it turns out to range from 528 to 26 500 μm with an average of 2740 μm, while the jet lengths (from inlet to breakup point) usually range from 200 to 1000 μm. This indicates that, as illustrated in Fig. 4, jet breakup in the gas–liquid system occurs within the developing region, with the quantitative comparison directly constraining alternative explanations by showing that the observed breakup locations are consistently shorter than the predicted developing lengths over a wide range of operating conditions. Figure 7 shows how the jet radius evolves in region II under different ΔCa values. The influence of ΔCa on the radius convergence pattern and the resulting LDR length can be clearly observed.

Furthermore, Fig. 7 reveals that the sign of ΔCa plays a decisive role in determining whether the jet exhibits contracting or expanding behavior. This is particularly interesting because the inlet radius of the jet is fixed by the microchannel design and fabrication, whereas the fully developed radius depends on flow rates and is independent of the inlet geometry. As a result, the relative size of the inlet and the developed radius can be reversed by altering the inlet geometry. Although, in practice, expanding jets rarely occur because of the typically high speed of the outer gas stream,[34] this scenario remains theoretically possible and finds support in the liquid–liquid systems. Since the contracting or expanding behavior of the jet is entirely determined by the inlet size and flow rates, it offers a useful way to verify predictions derived from the developing region. Figure 8 presents the comparison between two methods for predicting jet modes. It is assumed that the variation in jet radius is unidirectional, meaning that the radius either increases or decreases, corresponding to expanding jets and contracting jets. In Fig. 8, each combination of $R_{j,o}$, Ca_1, and Ca_2 corresponds to a specific point in the coordinate space. Points located above the fully developed radius curve correspond to contracting jets, while those below correspond to expanding jets. Alternatively, the jet

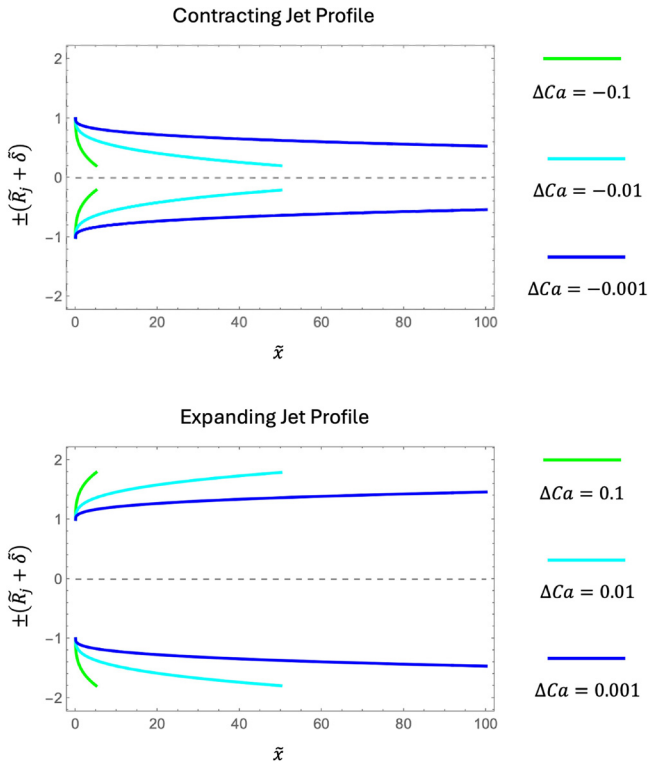

FIG. 7. Profile of expanding/contracting jets.

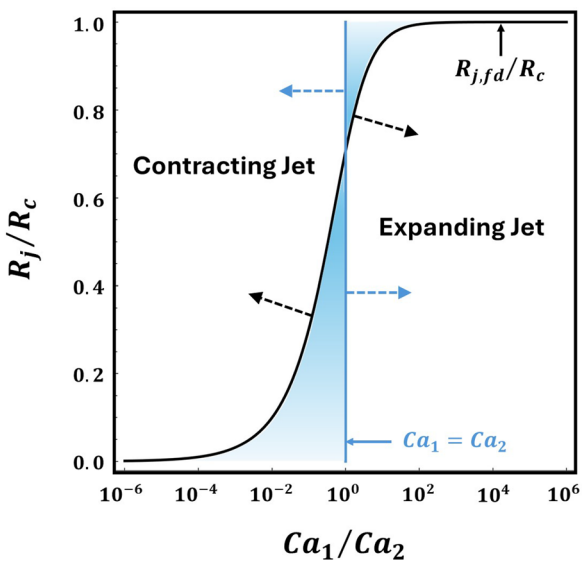

FIG. 8. Comparison between two methods for predicting expanding/contracting jet behavior: one based on the evolution of jet radius in the developing region, and the other based on the relationship between inlet radius and fully developed radius. The black curve represents the theoretical fully developed jet radius as a function of the *Ca* ratio. The blue line denotes the $Ca_1 = Ca_2$ contour. The blue-shaded area indicates regions where the two methods give conflicting predictions.

mode can also be judged by the position of the point relative to the line $Ca_1 = Ca_2$; points to the left represent contracting jets and those to the right represent expanding jets. The two methods generally show good agreement across most of the space, but inconsistent predictions appear as the *Ca* ratio approaches 1. This discrepancy is considered to arise from the assumption of unidirectional variation, which particularly neglects the role of region I. When the *Ca* ratio is close to 1, region I becomes the sole factor influencing the radius variation, potentially giving rise to complex jets,[19] such as expanding–contracting jets. Due to their complexity, such cases are not discussed further in this study.

B. Dispersion relation for developing region

According to Huerre's theory,[15] the dispersion relation of an open flow system holds the complete signature of its instability character. For the case of confined coaxial jets, a positive slope of complex frequency with respect to the complex wavenumber indicates that the system is absolutely unstable and defines the Dripping regime, where disturbances grow in place, droplets detach near the liquid inlet, and breakup is highly uniform but slow. A negative slope means that the system is convectively unstable and corresponds to the Jetting regime, where disturbances move downstream, a center jet forms, and breakup occurs farther away, yielding much higher throughput but broader droplet sizes. Absolutely unstable flow is governed by a single frequency with zero group velocity, producing monodisperse droplets, whereas convectively unstable flow involves several growing modes that prevent such precise control.

Unlike the one-dimensional nature of fully developed flows, the developing region is inherently two-dimensional. Recognizing the significance of this region, therefore, implies that dispersion relations derived for fully developed flows are no longer applicable. The developing pattern of the jet radius, rather than an explicit functional form, needs to be incorporated into the perturbation-response scenario, and thus, into the dispersion relation. Dispersion relations cannot, at least currently, be expressed merely by scaling laws, as no previous studies have taken this approach. Thus, two innovative approaches were adopted. First, a pseudo-fully developed assumption is introduced based on the combined insight from scaling analysis and numerical simulations. Region I is confined to a very short distance near the inlet, whereas actual jet breakup is consistently observed to occur within region II. In this downstream region, inertial effects are strongly attenuated, and the flow approaches a pseudo-fully developed state. Both the scaling results and COMSOL simulations show that, although the jet radius and pressure gradients have not yet reached their fully developed values, their variations along the streamwise direction become gradual. As a result, region II can be characterized by a fully developed like velocity profile coupled with a slowly evolving jet radius, which motivates the use of a pseudo fully developed assumption in the subsequent dispersion analysis.

Second, although Eq. (12) is a scaling pattern rather than an exact function, it remains appropriate to employ it in deriving rigorous relationships. Such use is not arbitrary. It can be seen that in numerous instances where scaling analysis has been applied to model fluid mechanics problems, the results obtained are often surprisingly accurate. Even in comparison to analytical solutions, the differences typically lie only in the accuracy of numerical coefficients. By introducing unknown coefficients into each of the three scaling steps used to obtain Eq. (12), the original scaling relation can be converted into an explicit

and usable mathematical model. This procedure preserves the structure dictated by the scaling analysis while allowing the resulting expression to be employed directly in the subsequent dispersion analysis. Thus, by introducing appropriate constant coefficients (a_1, a_2, and a_3) into the three scaling terms in Eq. (15), which are subsequently merged into two constants ($A_1 = \frac{a_1}{a_3}$ and $A_2 = \frac{a_2}{a_3}$) to form Eq. (16), a dispersion relation can be derived. Although this approach introduces two new degrees of freedom, these unknown coefficients are eventually determined in a straightforward manner with the aid of experimental results.

$$\tilde{\delta} = a_3 \cdot [(a_1 \cdot Ca_1 + a_2 \cdot Ca_2)\tilde{x}]^{1/3}, \tag{15}$$

$$\tilde{\delta} = [(A_1 \cdot Ca_1 + A_2 \cdot Ca_2)\tilde{x}]^{1/3}. \tag{16}$$

With the groundwork laid and the pseudo-fully developed assumption in place, the dispersion analysis can proceed, starting with the definition of a complete variable space: $\left(\frac{\partial P_1}{\partial x}, \frac{\partial P_2}{\partial x}, Ca_1, Ca_2, R_j\right)$, where $\frac{\partial P_1}{\partial x}$ and $\frac{\partial P_2}{\partial x}$ represent the pressure gradients of the inner and outer flows, Ca_1 and Ca_2 are their respective Capillary numbers, and R_j is the radius of the jet.

The use of the Capillary number as the velocity-related variable in the dispersion analysis is uncommon and, therefore, requires clarification. In the present framework, this choice is dictated by consistency with the scaling results obtained for the developing region, where the evolution of the jet radius is governed explicitly by the Capillary numbers. Since these scaling relations must be incorporated into the dispersion relation, one must either reformulate the scaling results in terms of velocity or flow rate or alternatively express the velocity and continuity relations in terms of the Capillary number. To maintain a consistent nondimensional formulation and to avoid redundancy in the variable space, the latter approach is adopted. Because the Capillary number is obtained through a linear transformation of the mean velocity under fixed fluid properties and channel geometry, it provides a natural nondimensional velocity scale for the dispersion analysis without introducing additional assumptions.

Following an approach similar to that employed by Guillot,[16,17] a small sinusoidal perturbation was introduced to each of the variables in the variable space, as shown in the flollowing equations, with all terms were normalized. $\tilde{x} = \frac{x}{R_{j,o}}$, $\tilde{k} = kR_{j,o}$, $\tilde{t} = \frac{t}{\tau}$, $\tilde{\omega} = \tau\omega$, $\tau = \frac{\mu_1 R_{j,o}}{\sigma}$, and $\frac{\partial \tilde{P}_i}{\partial x} = \frac{R_{j,o}^2 \frac{\partial P_i}{\partial x}}{\sigma}$. Under the assumption of linear instability, it is reasonable to assume that all perturbations share the same frequency and wavelength.

$$Ca_n = \overline{Ca_n} + \varepsilon_{Ca_n} e^{i(\tilde{k}\tilde{x} - \tilde{t}\tilde{\omega})}, \tag{17}$$

$$\frac{\partial \tilde{P}_n}{\partial x} = \overline{\frac{\partial \tilde{P}_n}{\partial x}} + \varepsilon_{P_n} e^{i(\tilde{k}\tilde{x} - \tilde{t}\tilde{\omega})}, \tag{18}$$

$$\tilde{R}_j = \overline{\tilde{R}_j} + \varepsilon_{R_j} e^{i(\tilde{k}\tilde{x} - \tilde{t}\tilde{\omega})}. \tag{19}$$

Two equations were derived by taking the total differential of the perturbations in the pressure gradients as follows:

$$\varepsilon_{P_1} = \varepsilon_{Ca_1} \frac{\partial \tilde{P_{1x}}}{\partial Ca_1} + \varepsilon_{Ca_2} \frac{\partial \tilde{P_{1x}}}{\partial Ca_2} + \varepsilon_{R_j} \frac{\partial \tilde{P_{1x}}}{\partial R_j}, \tag{20}$$

$$\varepsilon_{P_2} = \varepsilon_{Ca_1} \frac{\partial \tilde{P_{2x}}}{\partial Ca_1} + \varepsilon_{Ca_2} \frac{\partial \tilde{P_{2x}}}{\partial Ca_2} + \varepsilon_{R_j} \frac{\partial \tilde{P_{2x}}}{\partial R_j}. \tag{21}$$

Next, continuity equations were formulated for both inner and outer flows, leading to two additional equations, which describe the relationship between the jet radius and the Capillary numbers.

$$\tilde{k}\varepsilon_{Ca_1}\tilde{R}_j = -2\tilde{\omega}\varepsilon_{R_j}, \tag{22}$$

$$\tilde{k}\varepsilon_{Ca_2}\left(\tilde{R_c}^2 - \tilde{R_j}^2\right) = 2\tilde{\mu}\tilde{\omega}\tilde{R}_j\varepsilon_{R_j}. \tag{23}$$

Finally, the pressure gradients in the inner and outer regions were linked through the Laplace pressure, yielding a fifth equation as follows:

$$\varepsilon_{P_1} - \varepsilon_{P_2} = ik^3\varepsilon_{R_j} - ik\varepsilon_{R_j}. \tag{24}$$

By solving these five coupled equations [Eqs. (20)–(24)], the local dispersion relation was derived. The dependence of frequency on wavelength was found to consist of two components: a linear term with a coefficient α and a nonlinear term with a coefficient β,

$$\omega = i \cdot \beta\left(\tilde{k}^2 - \tilde{k}^4\right) + \alpha\tilde{k}. \tag{25}$$

Here, both α and β are functions of the parameters A_1, A_2, Ca_1, Ca_2, $\tilde{R}_c$, and $\tilde{\mu}$. The complete expressions of α and β are provided in Appendix B,

$$\alpha = \alpha\left(A_1, A_2, Ca_1, Ca_2, \tilde{R}_c, \tilde{\mu}, \tilde{x}\right), \tag{26a}$$

$$\beta = \beta\left(A_1, A_2, Ca_1, Ca_2, \tilde{R}_c, \tilde{\mu}, \tilde{x}\right). \tag{26b}$$

According to open flow instability theory, when the wavenumber k is taken to be real, the maximum value of the imaginary part of the frequency can be obtained. When this maximum is equal to zero, $\omega_{i,max} = 0$, the corresponding Capillary number (Ca) represents the critical threshold between the absolute and convective instability. Therefore, Eq. (29) can be used to describe the regime boundary in $Ca - Ca$ space.

$$\frac{\partial \tilde{\omega}_i}{\partial \tilde{k}} = 0 \rightarrow \tilde{\omega}_{i,\max} = \frac{\beta}{4}. \tag{27}$$

Let

$$\omega_{i.max} = 0. \tag{28}$$

Then,

$$\beta(Ca_1, Ca_2) = 0. \tag{29}$$

Recall that A_1 and A_2 are coefficients determined by the geometric cross-sectional characteristics of the inner and outer flows. The determination of these coefficients in the gas–liquid microfluidic system, with the aid of experimental data, will be discussed in later sections.

C. Effect of channel geometry on jet radius

Due to limitations in microfluidic chip fabrication accuracy, particularly along the "thickness" direction, the fabrication of fully enclosed circular coaxial microchannels is technically challenging. As a result, rectangular cross-sectional microchannels were designed and

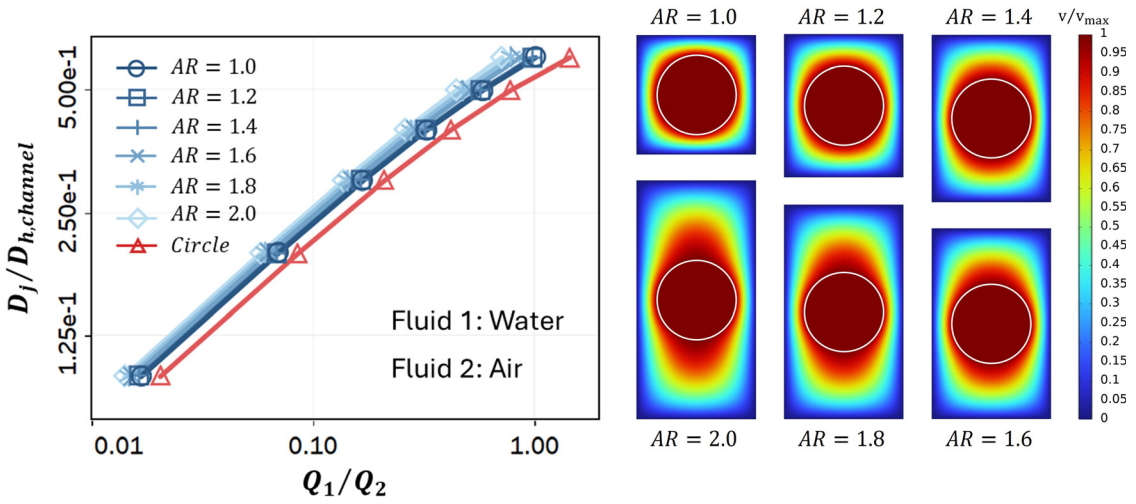

FIG. 9. COMSOL simulation results for rectangular channels with different aspect ratios. The left panel shows the nondimensional jet diameter as a function of the flow rate ratio for channels with varying aspect ratios. The right panel presents the cross-sectional velocity distributions for the corresponding channel geometries.

used in the experiments. This choice raises questions regarding the applicability of the jet theory developed above, which is based on axisymmetric circular channels and, therefore, requires an assessment of its applicability to rectangular geometries. A series of fluid dynamics simulations was conducted using COMSOL. The simulations compared fully developed jet diameters in channels with different aspect ratios (ARs) and examined the corresponding air-to-water flow rate ratios and velocity distributions across the cross section. The left panel of Fig. 9 shows the distribution of fully developed jet diameters in rectangular channels with AR ranging from one to two, over flow rate ratios from 0.01 to 1. Compared with circular channels, the jet diameter in rectangular channels is generally larger. The diameter increases with increasing AR, although the rate of increase gradually diminishes and converges to a value slightly larger than that in circular channels.

It should be noted that the simulations constrained the jet cross section to remain circular and did not account for possible shape deformation in rectangular channels, particularly at large ARs. The roundness of the jet cross section is inferred to depend on the competition between surface tension and the pressure gradient along the interface within the cross-sectional plane. When the Laplace pressure induced by surface tension greatly exceeds the maximum pressure difference along the interface, a circular jet shape is enforced. Otherwise, nonuniform internal pressure leads to an elliptical cross-sectional shape. A dimensionless parameter describing the degree of deviation from a circular shape (DDC) is, therefore, introduced and defined in the following equation:

$$DDC = \frac{\frac{1}{2}\rho(v_{max}^2 - v_{min}^2)R_j}{\sigma}. \tag{30}$$

By converting the velocity difference along the jet interface into a pressure difference and comparing it with surface tension, this parameter DDC is estimated to be ~0.014 as a maximum value among these rectangular channels, indicating a dominant role of surface tension. This result suggests that, for gas–liquid systems, the circular interface of the inner liquid jet is difficult to alter by asymmetry in the outer gas flow alone. As shown in the velocity contour plots on the right side of Fig. 9, velocity variations within the jet are negligible and remain below 5% for all aspect ratios, which explains why internal pressure variations are small compared with the Laplace pressure. These simulations and analyses indicate that, in terms of both shape and size, applying circular channel theory to fully developed air–water jets in rectangular channels introduces an acceptable level of error, with the predicted jet diameter being slightly underestimated. It should be noted that the simulations presented here focus on fully developed jets. However, the physical reasoning inferred from these results can be reasonably extended to region II of the developing flow. In this region, both the scaling analysis and numerical simulations indicate that the pressure gradients along the jet interface vary gradually, and the flow approaches a pseudo–fully developed state. As a result, the degree of deviation from circularity (DDC) in region II is expected to be comparable to that in the fully developed region (region III), supporting the validity of the circular jet assumption in this regime. In contrast, this assumption does not apply in region I. Very close to the inlet, the jet emerges directly from a rectangular channel cross section and undergoes rapid shape adjustment toward a circular interface. This process is driven by strong pressure gradients and pronounced curvature variation, making geometric effects unavoidable in region I. However, since jet breakup in the present study is consistently observed to occur within region II, and the dispersion relation is formulated specifically for this region, the limitations of the circular jet assumption in region I do not affect the validity of the present analysis. Once the flow transitions into region II, these effects are significantly attenuated, and the circular jet approximation becomes appropriate.

III. EXPERIMENTAL SETUP

A. Design and fabrication of microfluidic chips

As illustrated in Fig. 10, this work used a three-dimensional flow-focusing microchannel. The dispersed phase (liquid, subscript 1) enters through a central inlet, while the continuous phase (gas, subscript 2) arrives from two symmetric side channels. The three streams merge at

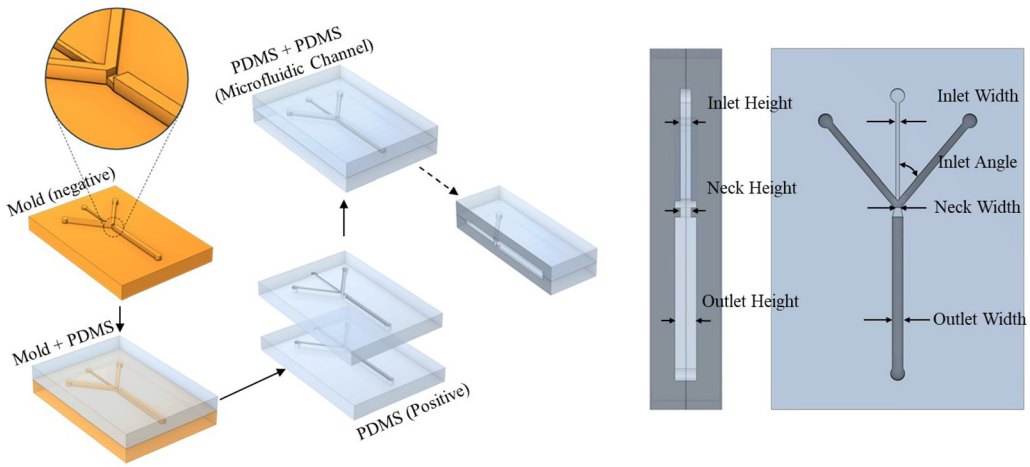

FIG. 10. The left panel shows the PDMS molding and bonding process used to fabricate the microfluidic chip. The schematic represents the geometry of the mold after the multi-layer lithography process, where SU-8 structures of different heights define the channel depths. PDMS is cast onto this mold, cured, and peeled off to obtain a PDMS piece with the channel pattern. Two identical PDMS pieces are then plasma-treated, aligned, and bonded to form the final enclosed chip. The right panel provides a side view and a top–down cross-sectional view of the chip, with key geometric parameters labeled, including the inlet channel width, neck width, main channel width, and height variations.

the neck, a converging–diverging section, before entering the main channel, where the flow phenomena of interest were observed. A multi-layer design gives the inlet and neck reduced height and the remaining sections greater height, enhancing flow-focusing and keeping the jet away from the walls. Key in-plane dimensions are the inlet width, the narrowest neck width, and the outlet channel width; key out-of-plane dimensions are the heights of the inlet, neck, and outlet channel. The gas and liquid inlets meet at a 60° angle. The channel geometries were combined into several chip types, summarized in Table I in Appendix A. Microchannels were fabricated by multilayer soft lithography. SU-8 was patterned on a silicon wafer to create a negative master. Polydimethylsiloxane (PDMS) was cast, cured, and peeled to form positive channel layers. Sequential photomask alignments left SU-8 of different thicknesses on the master, producing channels with defined depth variations. Two mirror-image PDMS layers were plasma activated, aligned, and bonded to yield the final 3D microfluidic chip with non-uniform heights.

Since PDMS is an elastomeric material, channel deformation under applied pressure is a potential concern in gas-driven microfluidic systems. Previous studies[38] on PDMS microchannels have shown that, under pressure drop of around 1 psi (the level measured in the present experiments), the maximum channel deformation at the location of highest pressure is ∼5%, which is generally considered acceptable for microfluidic applications. Under these conditions, the associated change in Capillary number scales with the square of the geometric deformation, leading to an estimated variation of ∼2.5%, which remains negligible in the context of the dispersion analysis. Therefore, elastic deformation of the PDMS channels is not expected to significantly alter the boundary conditions or affect the conclusions of this study.

B. Data acquisition (DAQ)

The experimental setup (Fig. 11) is centered on the microfluidic chip and divided into three coordinated modules:

Control module: A syringe pump (PHD 2000 Harvard Apparatus) delivers a steady liquid stream, while compressed, filtered air supplies the gas stream. A flow controller (up to 1 SLPM, Alicat Scientific) sets the total gas flowrate, and three fine valves adjust the inlet pressure and balance the two gas arms, ensuring reproducible flow conditions.

Measurement module: Two liquid flow meters (up to 80 and 1000 μl/min, Sensirion), two gas flow meters (Sierra Smarttrack 50), and two pressure transducers (Validyne) provide continuous analog output. These signals are routed to a multichannel DAQ (National Instruments USB-8452), where the custom MATLAB code converts the raw voltages using calibration factors, displays them in real time, and records time-stamped data for later analysis. Gas meters communicating over an RS-232 link are logged by a second script that follows the same workflow, so all sensor data share a common timeline.

Imaging module: A bright gooseneck lamp illuminates the chip, an optical microscope (Nikon Ti-U) focuses on the channel midplane, and a high-speed camera (Photron SA5) record synchronized videos of the flow. Time stamps based on the host computer's clock are used to align the camera frames with the log data, allowing direct correlation between visual and numerical data.

During each run, the two log scripts capture liquid-side flow, gas-side flow, and pressure signals without interruption. Afterward, a third script matches the video timestamps with the sensor log, assigns the clip indices, and exports a consolidated spreadsheet. MATLAB image-processing routines then classify the recorded flows into Jetting, Dripping, and Transition regimes, with additional sub-regimes identified by detailed breakup features.

IV. EXPERIMENTAL RESULTS

A. Regime map and instability

Deionized water was used as the liquid phase and dry air as the gas phase throughout all experiments with a surface tension of ∼0.072 N/m and a dynamic viscosity of 1.00 mPa s (water) and 1.81 $\times 10^{-2}$ mPa s (air) at room temperature. A complete regime map was

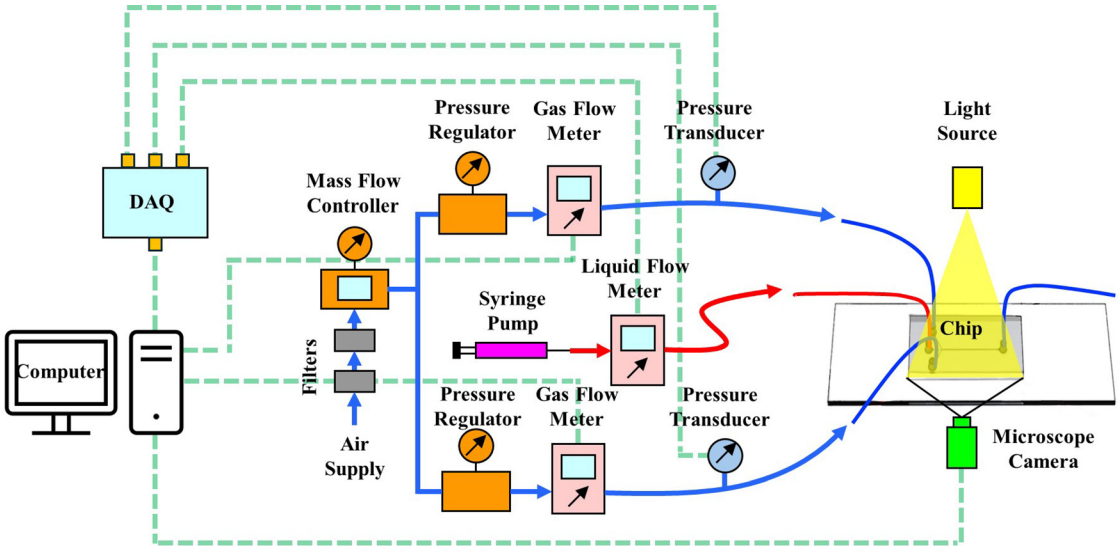

FIG. 11. Schematic diagram of the experimental platform.

obtained using a well-fabricated and well-aligned microfluidic chip, referred to as "*Chip a*," with gas flow rates ranging from 50 to 400 sccm and liquid flow rates ranging from 10 to 400 μl/min. Since the dispersion relation proposed in this study adopts the Capillary number as the velocity-related parameter rather than the volumetric flow rate, a dual axis representation was employed in the regime map, in which both volumetric flow rates and Capillary numbers were indicated. It should be emphasized that both variables are defined through linear transformations based on the mean velocities, while other parameters involved in their definitions, including channel dimensions, fluid viscosities, and surface tension, are treated as constants. As a result, the volumetric flow rate and Capillary numbers shown in the regime map reflect only the correspondence between mean velocities and flow regime and do not represent the influence of other parameters.

The regime map is shown on the left side of Fig. 12, where the Dripping regime occupies the lower left corner at low flow rates and low Capillary numbers. As the flow rates and Capillary numbers increase, Dripping transitions to Jetting across a regime boundary that can be described by a linear relation with a negative slope. This transition boundary, determined from a large set of experimental data, provides a key reference to identify parameters A_1 and A_2. Specifically, the regime boundary extracted from the map is fitted using a straight line and expressed in $Ca - Ca$ space in the form of Eq. (29), which allows A_1 and A_2 to be determined and, thus, completes the dispersion relation given by Eq. (25). It should be noted that, under this fitting procedure, determining both A_1 and A_2 from a single linear boundary relies on the independence of their influence on the two intercepts. This independence is a specific property observed in the present experiments and ensures that A_1 and A_2 can be uniquely determined using this approach. At the same time, it should be noted that the resulting values of A_1 and A_2 are valid only for the current regime map. Their applicability to different channel dimensions requires further investigation.

Following the fitting procedure described above, the parameters for the regime map shown in Fig. 12 were determined as $A_1 = 70$ and $A_2 = -45$. Based on these values, the dispersion relation for region II was obtained for *Chip a*, under air–water operating conditions. Within the Jetting regime, nine combinations of flow rates were selected, with air flow rates of 100, 150, and 300 sccm combined with water flow rates of 100, 150, and 300 μl/min. For each flow condition, the measured jet oscillation frequency was compared with the frequency predicted by the region II dispersion relation proposed in this study and with the frequency predicted by the fully developed region III model reported by Guillot.[16,17]

The comparison results are shown on the right side of Fig. 12. For all nine flow conditions, the frequency predictions based on region II show better agreement with the measured frequencies than those based on region III. This observation indicates that the pseudo-fully developed assumption adopted in this study, together with the corresponding theoretical framework, substantially reduces the frequency prediction error associated with fully developed models. The remaining discrepancy is likely related to the rectangular geometry of the channel and to the accuracy of the scaling approach. Future work will focus on addressing these factors and on developing more accurate predictive models.

Beyond instability classification and frequency selection, droplet size dispersion is also an important performance metric for gas–liquid microfluidic systems and is briefly discussed here for completeness. In the previous studies on gas–liquid microfluidic Dripping regimes,[11] droplet size dispersion was shown to remain on the order of 5% at low liquid Reynolds numbers. As the liquid Reynolds number increases, the appearance of satellite droplets leads to an increase in dispersion, although the primary droplet size distribution remains narrowly unimodal. This high level of uniformity is a direct consequence of the absolute instability governing the Dripping regime. In contrast, while the Jetting regime is attractive due to its significantly higher throughput, it is inherently governed by convective instability, which generally results in increased droplet size dispersion. Based on available observations, the dispersion level in the Jetting regime is estimated to be on the order of 25%. A more quantitative characterization is currently limited by

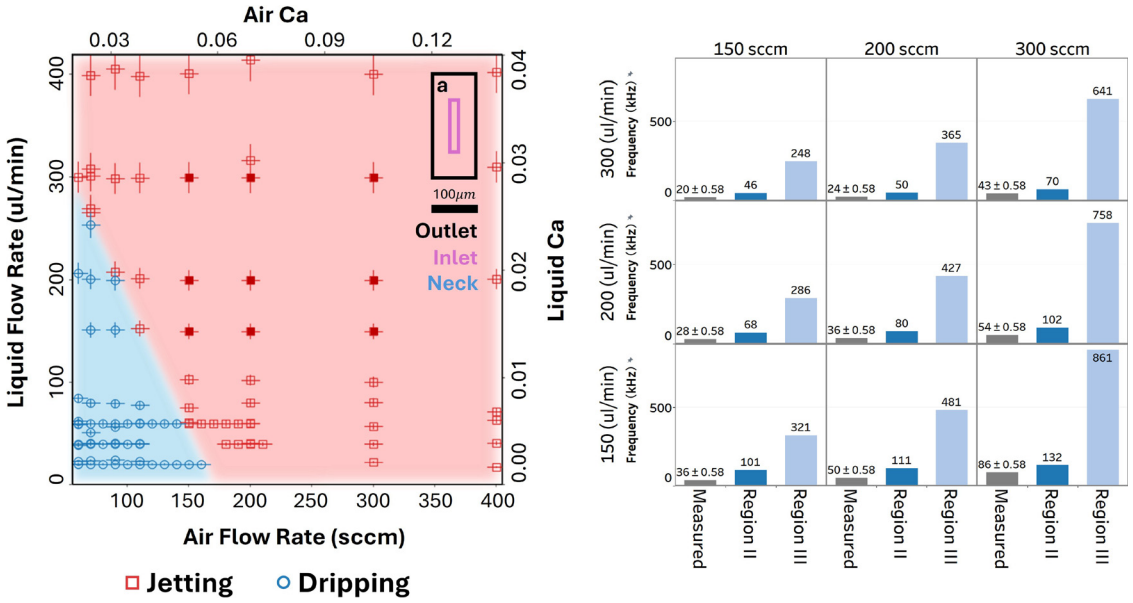

FIG. 12. Regime map and frequency comparison for *Chip a*. The left panel shows the experimentally obtained regime map. The right panel compares the measured jet oscillation frequencies with the frequencies predicted by the region II dispersion relation proposed in this study and by the fully developed region III model reported by Guillot[16,17] (cited here solely as the source of the theoretical model), for the nine selected flow rate combinations. The predicted frequencies are obtained from the corresponding dispersion relations by identifying the frequency associated with the maximum temporal growth rate, i.e., the cutoff frequency at which the imaginary part of the complex frequency reaches its maximum. The measured frequencies are extracted from high-speed jet videos using image-based signal processing and fast Fourier transform (FFT) analysis of the jet oscillations.

the temporal resolution of the imaging system used in this study. Nevertheless, it is well established that droplet uniformity in convectively unstable jets can be improved through controlled external forcing, such as acoustic or surface-wave excitation. The effectiveness of such control strategies relies critically on accurate prediction of the natural instability frequency, which motivates the present focus on developing a reliable dispersion relation for the developing region.

B. Effect of channel dimensions on A_1 and A_2

In Sec. II, to express the scaling results in an explicit mathematical form, three unknown coefficients, a_1, a_2, and a_3, were introduced. These coefficients were subsequently reduced to two parameters, A_1 and A_2, as shown in Eq. (16). The coefficients a_1 and a_2 originate from the scaling of the pressure drop within the two fluids in Eq. (9), while a_3 is associated with the scaling of the jet radius variation in Eq. (12). Together, these coefficients describe the scaling of the jet radius evolution along the flow direction. As shown in Fig. 8, the jet radius evolution not only converges toward the fully developed solution but is also strongly influenced by the initial condition, namely, the inlet channel dimension, which can substantially alter the overall development pattern. This observation suggests that A_1 and A_2 are parameters related to the relative ratio between the inlet and outlet channel sizes, representing a relative geometric relation rather than an absolute dimension.

To examine this dependence, two additional chips with geometries distinct from *Chip a* were designed, and the corresponding A values were determined experimentally. Compared with *Chip a*, *Chip b* incorporates a neck structure, while *Chip c* further increases the outlet channel width based on the design of *Chip b*. The resulting parameters are $A_1 = 189$ and $A_2 = -100$ for *Chip b*, and $A_1 = 267$ and $A_2 = -82$ for *Chip c*. As shown in the regime maps on the left side of Fig. 13, both new chips exhibit pronounced differences compared with *Chip a*, with the Dripping regime being significantly reduced.

A comparison between *Chip a* and *Chip b*, which share the same outlet channel size, shows that the presence of the neck alone shifts the regime transition location, consistent with the large deviation of the A values relative to *Chip a*. This behavior reflects the dominant role of the neck region, where Dripping typically occurs and where Jetting near the regime boundary is also primarily confined, making the neck geometry more representative than the outlet channel. Accordingly, *Chip b* and *Chip c*, despite having substantially different outlet channel sizes, yield similar level of A values due to their identical neck dimensions.

The same nine flow rate combinations were also used to compare the oscillation frequencies for the two additional chips, with the results shown on the right side of Fig. 13. The comparison indicates that a prediction error level similar to that observed for *Chip a* is also present for the two new chips. In addition, the frequency predictions based on region II exhibit an even smaller deviation from the measured values. These results demonstrate that, although the values of A_1 and A_2 vary significantly across different channel geometries, their effects are consistently captured by the region II dispersion relation. This agreement further supports the validity of the theoretical framework proposed in this study.

V. CONCLUSION

This work establishes a refined framework for analyzing instability in confined coaxial gas–liquid jets by systematically reconsidering

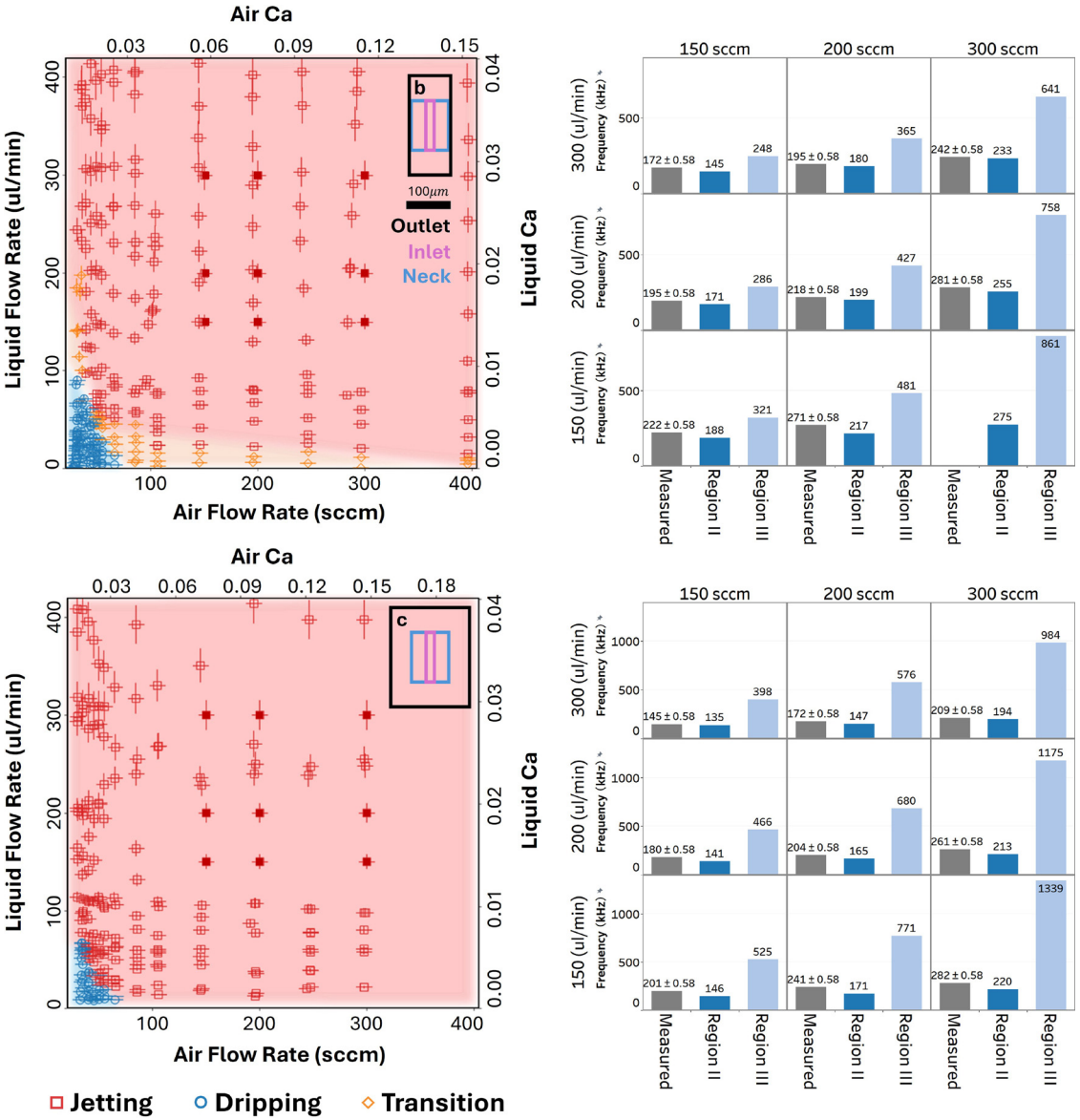

FIG. 13. Regime maps and frequency comparisons for *Chips b* and *c*. The left panels show the experimentally obtained regime maps for the two chips. The right panels compare the measured jet oscillation frequencies with the frequencies predicted by the region II dispersion relation and by the fully developed region III model, using the same set of flow rate combinations as in Fig. 12.

the role of the jet developing region. Through scaling analysis, the jet is divided into three characteristic regions based on the downstream evolution of the jet radius. It is shown that in gas–liquid systems the developing length (LDR) is significantly extended due to the low viscosity of the outer gas phase, rendering the fully developed flow assumption invalid in many practical scenarios. Jet breakup is shown to occur predominantly within the developing region, and more specifically within region II, where the jet radius evolves gradually under viscosity-dominated dynamics. The influence of inertial and viscous forces across regions I and II is revealed to govern the convergence of the jet radius, offering new insight into droplet formation mechanisms under confined geometries.

To incorporate these findings into instability analysis, a pseudo-fully developed velocity profile was constructed and introduced into the dispersion relation framework for region II. Although the model is built on scaling assumptions, it is rendered solvable by introducing a

limited number of unknown coefficients. These coefficients are not arbitrary fitted but are determined through experimentally measured regime boundaries, which anchor the dispersion relation while consistently accounting for variations in channel geometry. This approach, linking experimental regime mapping with theoretical structure, significantly improves predictive accuracy, particularly for dominant jet oscillation frequencies. Compared to classical models based on fully developed assumptions, the revised dispersion relation exhibits markedly better agreement with the measured jet dynamics.

Although the present formulation captures essential features of the developing region, it remains within the scope of a scaling approximation. Future efforts will focus on refining the mathematical description, particularly by further clarifying the transition between inertia-dominated and viscosity-dominated regimes and the coupled behavior across regions I and II. In addition, improving experimental capabilities, especially through higher frame rate imaging, will be crucial for extending the accessible frequency range and further validating the proposed theoretical framework.

ACKNOWLEDGMENTS

This work was partially supported by the National Science Foundation through CBET Award No. 1805244 (Fluid Mechanics Program). Additional support was provided by Northeastern University through discretionary and internal funding to the principal investigator.

AUTHOR DECLARATIONS

Conflict of Interest

The authors have no conflicts to disclose.

Author Contributions

Zihao Meng: Conceptualization (lead); Data curation (lead); Formal analysis (lead); Methodology (lead); Validation (lead); Visualization (lead); Writing – original draft (lead). **Carlos Hidrovo:** Conceptualization (supporting); Funding acquisition (lead); Methodology (supporting); Project administration (lead); Resources (lead); Supervision (lead); Validation (supporting); Writing – review & editing (lead).

DATA AVAILABILITY

The data that support the findings of this study are available from the corresponding author upon reasonable request.

NOMENCLATURE

Ca	Capillary number
$k/k_i/k_r$	Wave number/imaginary part/real part
l_{DR} and LDR	Fully developed jet length
l_j	Jet length
P	Pressure
Q	Volumetric flow rate
Re	Reynolds number
R_c	Main channel radius
R_j	Jet radius
$R_{j,fd}$	Fully developed jet radius
$R_{j,o}$	Initial jet radius
r	Coordinate components: Radical direction
u	Velocity x-direction component
v	Velocity/velocity r-direction component
We	Weber number
x	Cylindrical coordinate components: Flow direction
δ	Change of jet radius
$\epsilon_{\square}$	Amplitude of variable oscillation
θ	Coordinate components: Tangential direction
μ	Dynamic viscosity
ν	Kinematic viscosity
ρ	Density
σ	Surface tension
$\omega/\omega_i/\omega_r$	Frequency/imaginary part/real part
$\square_1$ ($\square_l$)	Property of inner (liquid) flow
$\square_2$ ($\square_g$)	Property of outer (gas) flow
$\square_n$ (n = 1 or 2)	Property of 1 or 2
$\square_{n,s}$ (n = 1 or 2)	Property of 1 or 2 on the interface
$\tilde{\square}$	Nondimensionalized variables

APPENDIX A: GEOMETRIC PARAMETERS OF 3D MICROFLUIDC CHIPS

Geometric parameters of different microfluidic chip types.

TABLE I. Geometric parameters of different microfluidic chip types.

Chip code	Outlet height (μm)	Outlet width (μm)	Neck height (μm)	Neck width (μm)	Inlet height (μm)	Inlet width (μm)	Inlet angle (deg)
*A*1	349	190	126	70	126	20	60
*A*2	349	190	126	90	126	20	60
*A*3	349	190	126	190	126	20	60
*B*1	118	130	80	70	80	20	60
*B*2	118	130	80	90	80	200	60
*C*1	190	100	140	25	140	20	60
*C*2	190	100	140	50	140	20	60
*D*1	245	100	126	90	126	20	60
Chip a	240	100	240	100	120	20	60
Chip b	240	100	120	90	120	20	60
Chip c	240	190	120	70	120	20	60

APPENDIX B: EQUATIONS

1. Equations for fully developed jet

$$\frac{\mu_n}{r}\frac{\partial}{\partial r}\left(r\frac{\partial u_n}{\partial r}\right)-\frac{\partial P_n}{\partial x}=0. \tag{B1}$$

$$\text{Boundary Conditions: } |u_1(r=0)|<\infty, \tag{B2a}$$

$$u_2(r=R_c)=0, \tag{B2b}$$

$$u_2(r=R_j)=u_1(R=R_j), \tag{B2c}$$

$$\mu_1\frac{\partial u_1}{\partial r}(r=R_j)=\mu_2\frac{\partial u_2}{\partial r}(r=R_j), \tag{C2d}$$

$$\frac{\partial P_1}{\partial x}=\frac{\partial P_2}{\partial x}, \tag{B2e}$$

$$\frac{\partial P}{\partial x}\left(\frac{R_j^2-R_c^2}{4\mu_2}+\frac{r^2-R_j^2}{4\mu_1}\right)=u_1(r), \tag{B3a}$$

$$\frac{\left(r^2-R_c^2\right)}{4\mu_2}\frac{\partial P}{\partial x}=u_2(r), \tag{B3b}$$

$$\frac{R_j}{R_c}=\sqrt{\frac{-\sqrt{\frac{\mu_2 Q_1}{\mu_1 Q_2}}+1+\frac{Q_1}{Q_2}+1}{-\frac{\mu_2}{\mu_1}+\frac{Q_1}{Q_2}+2}}. \tag{B4}$$

2. Equations for deriving dispersion relation

a. Continuity

Inner flow:

$$\pi\rho_1 R_j^2\Delta(u_1+\delta u_1)=\pi\Delta\rho_1 x\frac{\partial\left(\delta R_j+R_j\right)^2}{\partial t}, \tag{B5}$$

$$\tilde{R_j}^2\frac{\partial Ca_1}{\partial\tilde{x}}=\frac{\partial\left(\delta\tilde{R_j}+\tilde{R_j}\right)^2}{\partial\tilde{t}}, \tag{B6}$$

$$i\cdot\tilde{k}\delta Ca\tilde{R_j}^2=-2i\cdot\tilde{\omega}\tilde{R_j}\delta\tilde{R_j}, \tag{B7}$$

$$\tilde{k}\varepsilon_{Ca_1}\tilde{R_j}=-2\tilde{\omega}\varepsilon_{R_j}. \tag{B8}$$

Outer flow:

$$\rho_2\left(R_c^2-R_j^2\right)\Delta(u_2+\delta u_2)=\rho_2\Delta x\pi\frac{\partial\left[R_c^2-\left(\delta R_j+R_j\right)^2\right]}{\partial t}, \tag{B9}$$

$$\frac{\partial\delta Ca}{\partial\tilde{x}}(\tilde{R_c}^2-\tilde{R_j}^2)=\frac{-\partial\left(\delta\tilde{R_j}+\tilde{R_j}\right)^2}{\partial\tilde{t}}\tilde{\mu}, \tag{B10}$$

$$i\cdot\delta Ca_2\tilde{k}\left(\tilde{R_c}^2-\tilde{R_j}^2\right)=i\cdot 2\delta\tilde{\mu}\tilde{\omega}\tilde{R_j}\delta\tilde{R_j}, \tag{B11}$$

$$\tilde{k}\varepsilon_{Ca_2}\left(\tilde{R_c}^2-\tilde{R_j}^2\right)=2\tilde{\mu}\tilde{\omega}\tilde{R_j}\varepsilon_{R_j}. \tag{B12}$$

b. Laplace pressure

$$P_1-P_2=\frac{\sigma}{R_j}, \tag{B13}$$

$$(\delta P_1+P_1)-(\delta P_2+P_2)=\frac{\sigma}{\delta R_j+R_j}+\frac{\sigma}{-\left(\frac{\partial^2\delta R_j}{\partial x^2}\left\{1+O\left[\left(\frac{\partial\delta R_j}{\partial x}\right)^2\right]\right\}\right)}, \tag{B14}$$

$$\delta P_1-\delta P_2=\sigma\left(\frac{1}{\delta R_j+R_j}-\frac{\partial^2\delta R_j}{\partial x^2}-\frac{1}{R_j}\right), \tag{B15}$$

$$\delta P_{1x}-\delta P_{2x}=\sigma\left(\frac{1}{R_j^2}\frac{\partial\delta R_j}{\partial x}+\frac{\partial^3\delta R_j}{\partial x^3}\right), \tag{B16}$$

$$\delta\tilde{P}_{1x}-\delta\tilde{P}_{2x}=\delta\tilde{k}^3\tilde{R}-\delta i\tilde{k}\tilde{R}, \tag{B17}$$

$$\varepsilon_{P_1}-\varepsilon_{P_2}=ik^3\varepsilon_{R_j}-ik\varepsilon_{R_j}. \tag{B18}$$

c. Dispersion relation

$$\omega=i\cdot\beta\left(\tilde{k}^2-\tilde{k}^4\right)+\alpha\tilde{k}, \tag{B19}$$

where

$$\alpha=\frac{(A_2Ca_2-A_1Ca_1)\tilde{R_j}\left(\tilde{R_c}^2-\tilde{R_j}^2\right)}{\left(\tilde{R_j}-1\right)\left((A_1-A_2\tilde{\mu})\tilde{R_j}^2-A_1\tilde{R_c}^2\right)}, \tag{B20}$$

$$\beta=\frac{\left(\tilde{R_j}-1\right)^2\tilde{R_j}\left(\tilde{R_j}^2-\tilde{R_c}^2\right)}{2\left((A_1-A_2\tilde{\mu})\tilde{R_j}^2-A_1\tilde{R_c}^2\right)}. \tag{B21}$$

REFERENCES

[1] M. P. Boruah, P. R. Randive, and S. Pati, "Generation, migration, and coalescence of droplets: A state-of-the-art review from the perspectives of wettability, inertia, and electric field," Phys. Fluids **36**, 121301 (2024).
[2] Z. Jiang, H. Shi, X. Tang, and J. Qin, "Recent advances in droplet microfluidics for single-cell analysis," TrAC, Trends Anal. Chem. **159**, 116932 (2023).
[3] S. Pennathur, C. D. Meinhart, and H. Soh, "How to exploit the features of microfluidics technology," Lab Chip **8**, 20–22 (2008).
[4] S. Sadasivan, S. Pradeep, J. C. Ramachandran, J. Narayan, and M. J. Geca, "Advances in droplet microfluidics: A comprehensive review of innovations, morphology, dynamics, and applications," Microfluid. Nanofluid. **29**, 17 (2025).
[5] R. Fan, J. Wu, S. Duan, L. Jin, H. Zhang, C. Zhang, and A. Zheng, "Droplet-based microfluidics for drug delivery applications," Int. J. Pharm. **663**, 124551 (2024).
[6] D. Onan, M. Özder, M. İ. Sipahi, N. Poyraz, C. Apaydın, G. Erel-Akbaba, and H. Akbaba, "Microfluidics based particle and droplet generation for gene and drug delivery approaches," J. Biomed. Mater. Res. **113**, e35530 (2025).
[7] E. M. Payne, D. A. Holland-Moritz, S. Sun, and R. T. Kennedy, "High-throughput screening by droplet microfluidics: Perspective into key challenges and future prospects," Lab Chip **20**, 2247–2262 (2020).
[8] G. T. Vladisavljević, "Droplet microfluidics for high-throughput screening and directed evolution of biomolecules," Micromachines **15**, 971 (2024).
[9] W. Han and X. Chen, "A review on microdroplet generation in microfluidics," J. Braz. Soc. Mech. Sci. Eng. **43**, 247 (2021).
[10] C. Sharkey, R. White, M. Finocchiaro, J. Thomas, J. Estevam, and T. Konry, "Advancing point-of-care applications with droplet microfluidics: From single-cell to multicellular analysis," Annu. Rev. Biomed. Eng. **26**, 119 (2024).
[11] P. Tirandazi and C. H. Hidrovo, "An integrated gas-liquid droplet microfluidic platform for digital sampling and detection of airborne targets," Sens. Actuators, B **267**, 279–293 (2018).
[12] L. Nan, H. Zhang, D. A. Weitz, and H. C. Shum, "Development and future of droplet microfluidics," Lab Chip **24**, 1135–1153 (2024).

[13]J. Plateau, *Experimental and Theoretical Statics of Liquids Subject to Molecular Forces Only* (Gauthier-Villars, Paris, 1873).
[14]Lord Rayleigh, "On the stability, or instability, of certain fluid motions," Proc. London Math. Soc. **s1-11**, 57–72 (1879).
[15]P. Huerre and P. A. Monkewitz, "Local and global instabilities in spatially developing flows," Annu. Rev. Fluid Mech. **22**, 473–537 (1990).
[16]P. Guillot, A. Colin, A. S. Utada, and A. Ajdari, "Stability of a jet in confined pressure-driven biphasic flows at low Reynolds numbers," Phys. Rev. Lett. **99**, 104502 (2007).
[17]P. Guillot, A. Colin, and A. Ajdari, "Stability of a jet in confined pressure-driven biphasic flows at low Reynolds number in various geometries," Phys. Rev. E **78**, 016307 (2008).
[18]M. A. Herrada, A. M. Ganan-Calvo, and P. Guillot, "Spatiotemporal instability of a confined capillary jet," Phys. Rev. E **78**, 046312 (2008).
[19]L. Augello, A. Fani, and F. Gallaire, "The influence of the entry region on the instability of a coflowing injector device," J. Phys.: Condens. Matter **30**, 284003 (2018).
[20]K. Mu, G. Li, and T. Si, "Instability and interface coupling of coaxial liquid jets in a driving stream," Phys. Fluids **32**, 092107 (2020).
[21]Y. Liang, L. C. Johansen, and M. Linne, "Breakup of a laminar liquid jet by coaxial non-swirling and swirling air streams," Phys. Fluids **34**, 093606 (2022).
[22]Z. Wang, T. Zhai, H. Liu, Y. Huan, and W. Deng, "Two dimensional liquid flow focusing," Phys. Fluids **32**, 042104 (2020).
[23]C. Horvath, C. Arratia, and M. L. Cordero, "Measurement of the dispersion relation of a convectively unstable capillary jet under confinement," Phys. Fluids **27**, 114103 (2015).
[24]M. L. Cordero, F. Gallaire, and C. N. Baroud, "Quantitative analysis of the dripping and jetting regimes in co-flowing capillary jets," Phys. Fluids **23**, 094111 (2011).
[25]S. K. Jena, S. S. Bahga, and S. Kondaraju, "Prediction of droplet sizes in a T-junction microchannel: Effect of dispersed phase inertial forces," Phys. Fluids **33**, 032120 (2021).
[26]P. Tirandazi and C. H. Hidrovo, "Liquid-in-gas droplet microfluidics; experimental characterization of droplet morphology, generation frequency, and monodispersity in a flow-focusing microfluidic device," J. Micromech. Microeng. **27**, 075020 (2017).
[27]C. Barnes, A. R. Sonwane, E. C. Sonnenschein, and F. Del Giudice, "Machine learning enhanced droplet microfluidics," Phys. Fluids **35**, 092003 (2023).
[28]M. Jeyhani, M. Navi, K. W. Chan, J. Kieda, and S. S. Tsai, "Water-in-water droplet microfluidics: A design manual," Biomicrofluidics **16**, 061503 (2022).
[29]T. Gu, E. W. Yeap, A. Somasundar, R. Chen, T. A. Hatton, and S. A. Khan, "Droplet microfluidics with a nanoemulsion continuous phase," Lab Chip **16**, 2694–2700 (2016).
[30]M. T. Guo, A. Rotem, J. A. Heyman, and D. A. Weitz, "Droplet microfluidics for high-throughput biological assays," Lab Chip **12**, 2146–2155 (2012).
[31]A. Shahriari, M. M. Kim, S. Zamani, N. Phillip, B. Nasouri, and C. H. Hidrovo, "Flow regime mapping of high inertial gas–liquid droplet microflows in flow-focusing geometries," Microfluid. Nanofluid. **20**, 20 (2016).
[32]L. Sheng, Y. Chang, J. Wang, J. Deng, and G. Luo, "Hydrodynamics of gas–liquid microfluidics: A review," Chem. Eng. Sci. **285**, 119563 (2024).
[33]Z. Meng, C. Hidrovo, S. H. Maddila, M. Team *et al.*, "A local dispersion approach to gas-liquid microfluidic flow instability and droplet formation," in *APS Division of Fluid Dynamics Meeting Abstracts* (APS, 2024), pp. L20–008.
[34]Z. Meng, "Size analysis of the liquid thread in a gas-liquid droplet microfluidic device operating in the jetting regime," M.S. thesis (Northeastern University, 2021).
[35]B. Huang, X. Ge, B. Y. Rubinstein, X. Chen, L. Wang, H. Xie, A. M. Leshansky, and Z. Li, "Gas-assisted microfluidic step-emulsification for generating micron- and submicron-sized droplets," Microsyst. Nanoeng. **9**, 86 (2023).
[36]T. Si, F. Li, X.-Y. Yin, and X.-Z. Yin, "Modes in flow focusing and instability of coaxial liquid–gas jets," J. Fluid Mech. **629**, 1–23 (2009).
[37]K. Mu, R. Qiao, H. Ding, and T. Si, "Modulation of coaxial cone-jet instability in active co-flow focusing," J. Fluid Mech. **977**, A14 (2023).
[38]B. S. Hardy, K. Uechi, J. Zhen, and H. P. Kavehpour, "The deformation of flexible PDMS microchannels under a pressure driven flow," Lab Chip **9**, 935–938 (2009).